Realization of a scale of absolute spectral response using the National Institute of Standards and Technology high-accuracy cryogenic radiometer

T. R. Gentile, J. M. Houston, and C. L. Cromer

Using the National Institute of Standards and Technology high-accuracy cryogenic radiometer (HACR), we have realized a scale of absolute spectral response between 406 and 920 nm. The HACR, an electrical-substitution radiometer operating at cryogenic temperatures, achieves a combined relative standard uncertainty of 0.021%. Silicon photodiode light-trapping detectors were calibrated against the HACR with a typical relative standard uncertainty of 0.03% at nine laser wavelengths between 406 and 920 nm. Modeling of the quantum efficiency of these detectors yields their responsivity throughout this range with comparable accuracy.

1. Introduction

In a recent paper, measurements of the quantum efficiency of silicon photodiode light-trapping detectors obtained by using either the National Institute of Standards and Technology (NIST) high-accuracy cryogenic radiometer (HACR) or by using the NIST scale of detector spectral response were compared.[1] The excellent agreement obtained demonstrated HACR measurements at the level of accuracy of the detector response scale (relative standard uncertainty of 0.11%). The operation of the HACR has subsequently been automated to permit a larger number of measurements, and its accuracy has been analyzed in detail.[2] This study, along with the availability of a larger range of laser wavelengths, has permitted the realization of a detector response scale between 406 and 920 nm that is traceable to the HACR. This range of wavelengths was chosen for the first implementation of the HACR because the quantum efficiency of the silicon photodiode light-trapping detectors can be modeled accurately throughout this range.

To realize a scale of absolute spectral response, we used a combination of measurements and modeling. First, we calibrated the external quantum efficiencies of two silicon photodiode light-trapping detectors (hereafter referred to as trap detectors) at nine wavelengths between 406 and 920 nm by using five fixed-wavelength lasers and one tunable laser. Second, we obtained the external quantum efficiency throughout this wavelength range by using the following method.[3–5] The reflectance of each trap detector was measured at three wavelengths, from which the average oxide thickness on the constituent photodiodes was determined. Knowledge of the oxide thickness permitted the variation of the reflectance with wavelength to be calculated analytically.[6] The internal quantum efficiency was obtained by the use of the measured values of external quantum efficiency and the calculated reflectance. The variation of these data for the internal quantum efficiency with wavelength was then fitted with a model equation. The external quantum efficiency throughout the 406-nm to 920-nm range was then obtained by adding back the contribution of the reflection loss.

This paper is organized as follows. In Section 2 we describe the apparatus and the measurement procedure. The results of the measurements are presented in Section 3, and in Section 4 we discuss the analysis of the data. Conclusions are given in Section 5.

The authors are with the National Institute of Standards and Technology, Gaithersburg, Maryland 20899.

Received 14 August 1995; revised manuscript received 25 January 1996.

Table 1. Measured Values of η_e of Two Silicon Photodiode Light-Trapping Detectors

Air Wavelength (nm)	Laser	η_e Trap 1	η_e Trap 2	Combined Uncertainty[a] (%)
406.74	Kr^+	0.97534	0.97579	0.027
441.57	He–Cd	0.98530	0.98564	0.028
487.99	Ar^+	0.99100	0.99144	0.030
514.53	Ar^+	0.99264	0.99292	0.039
532.08	doubled Nd:YAG	0.99351	0.99363	0.042
632.82	He–Ne	0.99578	0.99597	0.034
769.64	Ti–sapphire	0.99636	0.99661	0.029
828.30	Ti–sapphire	0.99647	0.99660	0.027
919.85	Ti–sapphire	0.99611	0.99618	0.029
950.95	Ti–sapphire	0.9906	0.9910	0.08

[a]The combined relative standard uncertainty at each wavelength is the sum (in quadrature) of the type A and combined type B uncertainties listed in Table 2.

2. Apparatus and Measurement Procedure

A. High-Accuracy Cryogenic Radiometer

As the HACR has been described in detail elsewhere,[2,7] here we provide only a brief overview of the instrument. The HACR is an electrical-substitution radiometer that is operated just above the boiling point of liquid helium. An electrical-substitution radiometer links a measurement of optical power to the watt by comparing the temperature rise induced in an absorbing mass by incident optical radiation with that obtained by electrical heating. The absorbing mass is a cavity that is designed for nearly complete absorption of laser radiation. Operation at cryogenic temperatures permits a large, highly absorptive cavity to be used without degrading the time constant, and it reduces the radiative coupling of the cavity to its surroundings. However, a vacuum must be maintained in the HACR Dewar, which requires a window between the cavity and the laboratory. To reduce the reflection loss to a small value, the polarized laser beam enters the radiometer through a window that is oriented at Brewster's angle. The HACR can measure the power of a collimated beam of optical radiation with a combined relative standard uncertainty of 0.021% for an optical power level of 0.8 mW.

B. Optical Sources

The HACR is designed to be used with a beam of collimated, polarized light with a typical power level of 0.8 mW. In addition, it is convenient when silicon photodiode detectors are used for the bandwidth of the light to be smaller than ~0.01% of the wavelength. Because the internal quantum efficiency of silicon photodiodes is nearly 100% at visible wavelengths, their spectral response increases roughly linearly with wavelength. Hence for these detectors to be calibrated with a given accuracy, either the wavelength must be known to that accuracy or the spectrum of a broad source must be well characterized; the former is more convenient. These considerations lead one to the use of laser sources.

The lasers that were employed for these measurements are listed in Table 1. (Although the titanium–sapphire laser can be tuned from 700 to 1050 nm, we have listed only those wavelengths at which we performed measurements.) For the argon-ion (Ar^+), helium–neon (He–Ne), and doubled Nd:YAG lasers, an interference filter was placed in the optical path to eliminate light with undesired wavelengths. (This could be broadband emission from the laser tube discharge in the case of the Ar^+ and He–Ne lasers or residual light at the fundamental wavelength in the case of the doubled Nd:YAG laser.) For the helium–cadmium (He–Cd), krypton-ion (Kr^+), and titanium-sapphire (Ti–sapphire) lasers, a Pellin–Broca prism was placed in the beam path. In the case of the He–Cd laser, this prism was used to deflect unwanted 325-nm light that was emitted simultaneously with the 442-nm light. For the Kr^+ and Ti–sapphire lasers, the prism was used to reject broadband amplified spontaneous emission. (Measurements with the Ti–sapphire laser operating at a wavelength of 770 nm were also performed without the prism for comparison. The results for the external quantum efficiency were the same, within uncertainties, as the data obtained with the prism, indicating that the effect of any amplified spontaneous emission was small.) The Ar^+ and Kr^+ lasers were both operated with an intracavity prism that only permitted lasing on the chosen line. The wavelength of the Ti–sapphire laser was measured with a wavemeter and was typically stable to within ±0.005% over the course of a day.

C. Transfer Devices: Silicon Photodiode Light-Trapping Detectors

As the trap detectors used as transfer devices have also been described elsewhere,[1,4,8,9] here we only briefly review their characteristics. A photodiode trap detector is an arrangement wherein the optical radiation reflected by a photodiode is intercepted by other photodiodes. The design of the trap detector we have employed for this scale realization is shown in Fig. 1. It consists of three windowless, 1 cm × 1 cm photodiodes[10] arranged such that the incident light undergoes five reflections and exits the entrance of the trap detector along the path of the incoming beam. The angle of incidence is 45° for the first, second, fourth, and fifth reflections and 0° for the third reflection. For the response of the trap detector to be insensitive to the polarization of the incoming light, the second and fourth reflections are in a plane orthogonal to the plane of the first and fifth reflections. The photodiodes are enclosed in a metal box with a 13-mm-diameter entrance aperture. The responsivity of trap detectors is linear to within 0.01% up to 1 mW of incident optical power, insensitive to temperature (less than 0.02%/K), and spatially uniform (less than 0.02% variation over a 2-mm spot).

The reflectance of the trap detectors is typically below 0.4% over most of the wavelength range under study but increases to 1.0% at 406 nm. Because of the low value of the reflectance, the responsivity of a trap detector is insensitive to changes in the reflectance, such as those that can be caused by variations in the quantity of absorbed water on a single photodiode.[11]

The three photodiodes in the trap detector are connected in parallel so as to sum the photocurrents. The total photocurrent is input to a transimpedance amplifier that is operated with a gain of 10^4 V/A. The typical output voltage for 0.8 mW of incident laser light is between 2.6 V (at 406 nm) and 5.9 V (at 920 nm) and is measured with a high-accuracy digital voltmeter.

D. Optical System and Measurement Sequence

The optical system to perform measurements with the HACR is also described in Gentile *et al.*[2] The trap detectors are mounted on a computer-controlled, motor-driven carousel, which positions the detectors in the optical beam. An algorithm is used to determine the position of each trap detector for measurements; these locations are then accessed by the computer program used for automated HACR measurements. The procedure for the initial positioning of each trap detector is as follows. First, the trap detector is positioned manually by finding the rough center of the response of the trap detector with respect to translations along the two axes transverse to the beam, one radial (movement of the center of the carousel) and the other tangential (rotation of the carousel). The trap detector is also oriented so that the angle of the reflected beam is within 0.01 rad of the incident beam. Then the trap detector is translated along one axis under computer control to determine the locations at which the trap detector signal decreases to 80% of its maximum value. The trap detector is then positioned midway between these two locations, and the procedure is repeated for the other axis. The typical beam diameter at the trap detector was 2–3 mm.

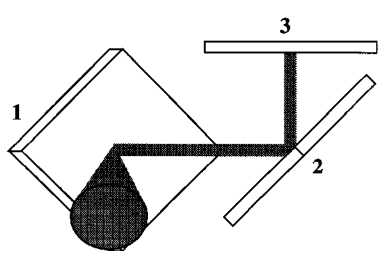

Fig. 1. Design of the silicon photodiode light-trapping detectors.

The details of the automated sequence for the HACR measurements are described in Gentile *et al.*[2] Briefly, the sequence consists of one optical measurement cycle, in which the temperature rise of the cavity caused by the laser light is determined, and two electrical heating cycles, in which the quantity of electrical power required to reproduce this temperature is determined. Measurements of the response of the trap detectors were integrated into the HACR automation sequence and performed during the first electrical heating cycle.

3. Measurement Results and Uncertainties

A. Results

The external quantum efficiency of the trap detector, η_e, is the number of photoelectrons that contribute to a measurable current, divided by the number of incident photons. Hence it is given by

$$\eta_e = \frac{hc}{en\lambda} S, \tag{1}$$

where S is the measured responsivity (photocurrent per unit optical power), λ is the air wavelength of the incident light, n is the index of refraction of air, h is Planck's constant, c is the speed of light in vacuum, and e is the electronic charge. Using values $h = 6.62608 \times 10^{-34}$ J s, $c = 2.99792 \times 10^8$ m/s, $e = 1.60218 \times 10^{-19}$ C, and $n = 1.00029$ yields

$$\eta_e = 1239.48\left(\frac{S}{\lambda}\right) \tag{2}$$

for λ in nanometers. (The variation in n between 406 and 920 nm is only 0.001%, which is negligible.) In terms of the actual measured quantities, S is given by $S = V/GP_L$, where V is the measured output voltage from the transimpedance amplifier, G is the gain of this amplifier in volts per ampere, and P_L is the optical power measured by the HACR (L refers to laser).

The results of our measurements of η_e at ten wavelengths are listed in Table 1 for both trap detectors and plotted in Fig. 2 for trap detector 2. For the small lasers that were operated overnight (He–Cd, Ar^+, doubled Nd:YAG, and He–Ne), the values in Table 1 represent the average of between 40 and 80 measurements of η_e, obtained in 2–4 nights of data acquisition. For the larger lasers that were operated only in the daytime (Kr^+ and Ti–sapphire), from six to 30 measurements were averaged, obtained over the course of 1–4 days. We have monitored η_e at the 633-nm wavelength over a period of 3 yr and found it to be constant to within 0.02%.

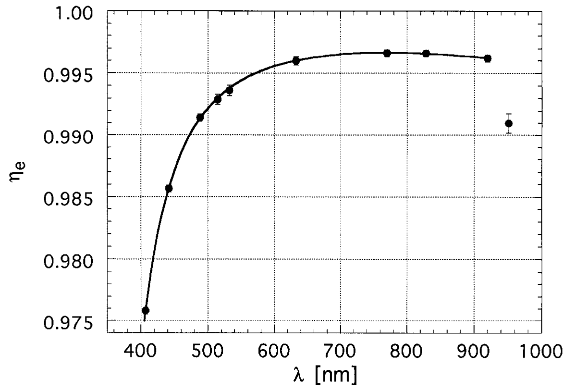

Fig. 2. Measured values of η_e for trap detector 2 (filled circles), with error bars equal to the uncertainties listed in Table 1. The solid curve shows $\eta_e(\lambda)$, which is the result of modeling the variation of η_e with wavelength in the range between 406 and 920 nm (see Section 4).

The reader will note the substantially higher uncertainty in the data point at 951 nm. We performed only a quick measurement at 951 nm to establish that we had reached the precipitous decline in η_e that occurs in this wavelength range. The uncertainties are higher because we experienced some difficulties in the operation of our Ti–sapphire laser at this wavelength, and the correction for the window transmittance was higher (because of an absorption feature in fused silica). Because we do not expect to model accurately the rapid decline in η_e with increasing wavelength that occurs in this range, we do not include this data point in our modeling. The only exception is at the end of the paper, where we briefly discuss modeling this long wavelength range.

B. Uncertainties

The components of the combined uncertainties listed in Table 1 can be found in Table 2. They are divided into type A and type B uncertainties.[12] (Type A and type B distinguish between uncertainties that are determined by statistical methods or other methods, respectively.) All uncertainties in the quantum efficiency data discussed in this paper are relative standard uncertainties and are often referred to simply as uncertainties. The combined uncertainty is dominated by the uncertainty in the measurement of P_L by the HACR. A detailed analysis of the uncertainties in the measurement of optical power by the HACR can be found in Gentile *et al.*[2] Although our discussion here is abbreviated, we discuss the procedure that was used to apply a small nonequivalence correction to the data in this paper.

1. *Type B Uncertainties in* $\mathrm{P_L}$

The optical power, P_L, is given by

$$P_L = \frac{1}{T}\left(\frac{NP_H}{A} + P_S\right), \tag{3}$$

where P_H is the electrical heater power that yields the same temperature rise in the cavity as that produced by the optical beam, P_S is the estimated optical power scattered out of the field of view of the cavity, A is the absorptance of the cavity, T is the transmittance of the entrance window of the HACR, and N is a factor to take into account any nonequivalence between the optical and electrical heating. (As in Gentile *et al.*,[2] we use the term nonequivalence to refer to any difference between the response of the HACR for the optical and electrical cycles.) The typical value of T was 0.9997. The uncertainty components in T

Table 2. Components of the Combined Relative Standard Uncertainty in η_e for Each Wavelength Listed in Table 1

Wavelength (nm)	T (%)	P_S (%)	P_L[a] (%)	Temperature (%)	Combined Type B (%)	Type A (%)	Wavelength-independent uncertainty components (%)
406.74	0.006	0.002	0.019	0.008	0.023	0.016	
441.57	0.011	0.010	0.023	0.006	0.026	0.012	
487.99	0.011	0.009	0.023	0.005	0.026	0.016	
514.53	0.011	0.012	0.024	0.003	0.026	0.030	
532.08	0.025	0.011	0.033	0.003	0.035	0.024	
632.82	0.021	0.010	0.030	0.003	0.031	0.013	
769.64	0.017	0.004	0.025	0.002	0.027	0.009	
828.30	0.018	0.009	0.021	0.002	0.024	0.013	
919.85	0.021	0.004	0.023	0.002	0.025	0.015	
950.95	0.067	0.005	0.068	0.006	0.069	0.045	
Other components of uncertainty in P_L							
N_d[b]							0.016
N_i							0.004
Other HACR uncertainties							0.006
Amplifier gain (G)							0.01
Voltage measurement (V)							0.003
Nonuniformity							0.003

[a]The uncertainty in P_L includes the uncertainty components in T, P_S, and the applicable wavelength-independent components.
[b]This contribution is not applicable to data at 828.30, 919.85, and 950.95 nm.

and P_S are listed for each wavelength in Table 2. The deviation of absorptance A from unity is a small correction and is simply included in the category for other HACR uncertainties in Table 2. The reader is referred to Gentile *et al.*[2] for more detailed information on the column labeled other HACR uncertainties in Table 2.

Two nonequivalence errors were found during the course of these measurements. Although they have been eliminated, they affected the data for this scale realization. One contribution (labeled N_i) was independent of the optical power, whereas another was power dependent (labeled N_d). N is given by $N = N_i N_d$. The power-independent contribution was not discovered until after the scale realization was completed; hence it applies to all of the data in this paper. The power-dependent contribution was discovered and eliminated part of the way through this scale realization, so it only applies to some of the data. As described in Gentile *et al.*,[2] $N_i = 0.99992 \pm 0.00004$, and its origin was a small transient that injected power into the HACR's electrical heater circuit when the multiplexing digital voltmeter read the signal from the transimpedance amplifiers. The magnitude of N_d depends on wavelength only because different optical power levels were used for each wavelength. While N_d varied between 0.99995 and 0.99967, the uncertainty component was independent of wavelength; hence it is listed in Table 2, along with the uncertainty component for the power-independent contribution. We now describe the power-dependent contribution in more detail.

As described in Gentile *et al.*,[2] a small nonequivalence error was found that was rooted in a different level of background heating of the HACR cavity in the optical cycle, as compared with the electrical cycles. The background heat difference was rooted in electrical transients that were produced by the instrumentation for the HACR thermometry. (Here background refers to sources other than the optical or electrical heating.) This difference produced a systematic dependence of the measured external quantum efficiency, η_m, on the measured optical power, P_m. (Subscript m is used only in this discussion; P_m refers to the value of P_L that is obtained with $N = 1$.) This effect was studied through a series of measurements at 633 nm, where we found that the variation of η_m with P_m was well fit by

$$\eta_m = B\eta \frac{P_m - C}{P_m}, \tag{4}$$

where η and C are fitting parameters that correspond to the true external quantum efficiency and the difference in background heating, respectively; B is discussed below. These data and the fit to Eq. (4) are shown in Fig. 3. After eliminating the cause of the nonequivalence error, we verified that η_m was independent of P_m within the uncertainties of our measurements. These data are also shown in Fig. 3; for these results, $\eta_e = \eta_m$. Comparing values η_e and η provided a check of the accuracy with which the fitting procedure could be used to extract the true quantum efficiency. We found that η_e and η differed by 0.015%. To take account of this discrepancy, we introduced the additional fitting parameter, B, that was adjusted so that η agreed with η_e. The value of B was found to be 1.00015 ± 0.00003.

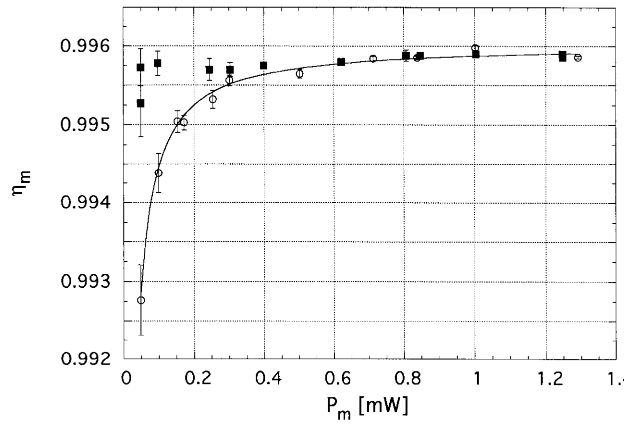

Fig. 3. Effect of the power-dependent nonequivalence error on η_m (at 633 nm). The open circles (filled squares) show data taken before (after) the nonequivalence error was eliminated. At low values of P_m, where the type A uncertainty dominates, the error bars represent the standard deviation of the mean. The solid curve shows the result of fitting the data shown by open circles to Eq. (4).

Because this nonequivalence error is associated with a background thermal load on the cavity, the effects are independent of wavelength. To correct for this nonequivalence error at other wavelengths, we note that Eq. (4) implies a value of N_d given by

$$N_d = B \frac{P_m - C}{P_m}; \tag{5}$$

hence N_d depends on the optical power. (We have neglected the slight difference between P_L and P_H.) To evaluate N_d, we used the fitted values of C and B that had been determined from the above study at 633 nm. Because the deviation of B from unity is a contribution to the uncertainty in N_d, the combined uncertainty in N_d was determined by adding an uncertainty of 0.015% in quadrature with the components from the uncertainties in fitting parameters C and B. For the optical power levels of our measurements, the uncertainties in N_d were dominated by the fixed 0.015% contribution.

The component of uncertainty arising from the combined type B uncertainty in P_L is listed for each wavelength in Table 2. It was calculated by summing (in quadrature) the uncertainty components from T, P_s, N_d, N_i, and the category labeled "Other HACR uncertainties" in Table 2.

2. *Other Type B Uncertainty Components*

Other type B uncertainty components are from the uncertainty in the gain of the transimpedance amplifiers, the accuracy of the digital voltmeter, and the temperature dependence and spatial nonuniformity of the responsivity of the photodiodes. The gains of the transimpedance amplifiers were determined by measuring the voltage output for a known input current and were all found to be within 0.013% of 10^4 V/A. The contribution from the temperature dependence of the responsivity was calculated by using the temperature coefficient data in Lei and Fischer[8] and Kohler *et al.*[9] The laboratory temperature was 295.5 ± 0.5 K.

Because of the excellent spatial uniformity of the trap detectors and the repeatability of the positioning algorithm, the uncertainty caused by nonuniformity is small. In a series of tests at 633 nm involving only the trap detectors, we measured the variation in the trap detector response caused by changes in the position and diameter of the laser beam. For ±0.5-mm translations of the beam or ±1-mm changes in the diameter (range from 2 to 4 mm), the maximum relative change in the output of the trap detectors was ±0.006%; we have assigned a relative standard uncertainty caused by nonuniformity of half this value. The combined type B uncertainty is listed in Table 2 for each wavelength. We calculated it by summing (in quadrature) the uncertainty component in P_L with these other uncertainty components (gain, voltage, temperature, and nonuniformity).

We tested the sensitivity of η_e to the polarization of laser light at a wavelength of 406 nm and found a maximum relative difference of 0.04% for orthogonal linear polarizations. Because polarization sensitivity would arise from reflectance sensitivity, this should yield a worst-case test because the reflectance is the highest at this wavelength. Because the trap detectors are always calibrated with the same orientation with respect to the polarization, this difference is not included in the uncertainty budget but would be applicable to the uncertainty in transferring this calibration to a system with unpolarized light or light with a different direction of polarization.

3. *Type A Uncertainty Components*

The relative standard deviation of repeated measurements of η_e during a session of data acquisition is listed for each wavelength in Table 2. (The values are not the standard deviation of the mean.) Because the trap detector–amplifier system is highly stable and has low noise, these uncertainties are dominated by the type A uncertainty in the measurement of P_L. Differences among the wavelengths were primarily due to variations in laser power and stability. (As described in Gentile *et al.*,[2] the type A relative standard uncertainty in the measurement of P_L is inversely proportional to the laser power.)

4. Analysis and Realization of a Scale

To realize a scale of absolute spectral response, we used our measurements at discrete wavelengths in conjunction with calculations and modeling to determine η_e at all wavelengths between 406 and 920 nm, which we refer to as $\eta_e(\lambda)$. We accomplished this by first determining $R_t(\lambda)$ and $\eta_i(\lambda)$, the wavelength dependences of the trap detector reflectance and internal quantum efficiency, respectively, and then combining them to form $\eta_e(\lambda)$.

Assuming that the internal quantum efficiency is the same for each photodiode in the trap detector, we find that external quantum efficiency η_e is given by

$$\eta_e = \eta_i(1 - R_t), \tag{6}$$

where η_i is the internal quantum efficiency and R_t is the reflectance of the trap detector. As shown in Fig. 2, η_e exhibits a slow decline for wavelengths shorter than ~600 nm and a steep decline for wavelengths longer than ~920 nm. Although the slow decline at short wavelengths is due to a combination of increased reflectance and decreased internal quantum efficiency, the steep decline at long wavelengths is entirely due to decreasing internal quantum efficiency. The decline of the internal quantum efficiency at both ends of the spectrum is related to the behavior of the absorption coefficient for silicon.[13] For short wavelengths (~400 nm), the light is absorbed in a shallow region near the Si–SiO_2 interface, where the recombination rate of the carriers is higher than in the remainder of the photodiode. This reduces the number of carriers that cross the junction and contribute to the photocurrent and hence decreases the internal quantum efficiency. For wavelengths beyond ~950 nm, the absorption depth is greater than the thickness of the photodiode, so fewer electron-hole pairs are generated. At wavelengths between 750 and 950 nm, a slow decline in quantum efficiency is expected because some electron-hole pairs are generated far behind the junction, and recombination may prevent them from crossing the junction. To model the behavior of the internal quantum efficiency, we must first determine $R_t(\lambda)$.

A. Trap Detector Reflectance

The reflectance of the trap detector is given by $R_t = [R_p(45°)\ R_s(45°)]^2 R(0°)$, where $R_p(45°)$ and $R_s(45°)$ are the reflectances for light incident at an angle of 45° to a given photodiode and polarized parallel and perpendicular to the plane of incidence of the reflection, respectively, and $R(0°)$ is the normal incidence reflectance. We calculated the reflectance for the air–SiO_2–Si interface at the surface of the photodiode by using an analytical formula for the reflectance [Eq. (30) of Chapter 13 of Born and Wolf[6]]. This reflectance formula requires the real and imaginary parts of the index of refraction of silicon (see Appendix A), the real part of the index of refraction of SiO_2,[14] and the oxide thickness. To determine the oxide thickness, we measured the reflectance of each trap detector at 406, 532, and 633 nm and fit the value of the oxide thickness that was used in the reflectance formula so as to obtain the best agreement with the reflectance data for each trap detector.

Whereas the reflectance measurements had a typical relative uncertainty of 0.5% or smaller, we found that the relative errors between the data and the results of the fit were typically between 1% and 3.6%. Possible sources for this discrepancy are a component

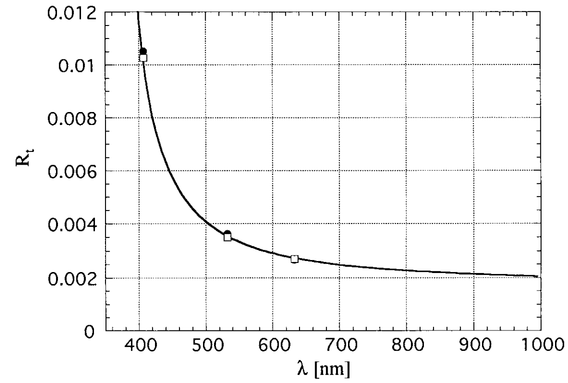

Fig. 4. Variation of reflectance R_t of the trap detectors with wavelength. The data for the two trap detectors are shown by open squares (trap 1) and filled circles (trap 2), and the solid curve is $R_t(\lambda)$, which is the reflectance calculated from the analytical formula in Born and Wolf,[6] using a oxide thickness of 28.05 nm.

of diffuse reflectance or inadequacies in the calculation, such as errors in the refractive index data or the use of an average thickness for all the constituent photodiodes in the trap detector. To obtain a reduced χ^2 near 1,[15] we enlarged the uncertainties in the measured values of R_t. The resulting fitted values of the oxide thickness were 28.12 ± 0.35 nm for trap 1 and 27.98 ± 0.35 nm for trap 2, where we determined the uncertainties by varying the oxide thickness until χ^2 increased by 1. Because these two values agreed well within their uncertainties, we chose a single, average oxide thickness of 28.05 ± 0.42 nm. The reflectance data for both trap detectors and calculated reflectance $R_t(\lambda)$ are shown in Fig. 4 and listed in Table 3. We determined values for η_i, also listed for each wavelength in Table 3, by using the data for η_e (listed in Table 1) and the values of $R_t(\lambda_k)$, where subscript k refers to the wavelengths of our measurements. We derived the uncertainty in each value of $R_t(\lambda_k)$ from the 0.42-nm uncertainty in determining the oxide thickness in conjunction with the analytical equation for the trap detector reflectance. The combined relative uncertainty in η_i includes components from both η_e and $R_t(\lambda_k)$, where the relative uncertainty component for $R_t(\lambda_k)$ is small because it is approximately equal to the absolute uncertainty in $R_t(\lambda_k)$. The uncertainty in the values of $R_t(\lambda_k)$ only affected the final result for $\eta_e(\lambda)$ through the modeling of the values of η_i. This is because we used $R_t(\lambda)$ both to extract η_i from each data point for η_e and, after $\eta_i(\lambda)$ was obtained from fitting the values of η_i, to determine $\eta_e(\lambda)$ from $\eta_i(\lambda)$.

B. Modeling the Internal Quantum Efficiency

Modeling the variation of the internal quantum efficiency with wavelength in the 400-nm to 900-nm wavelength range has been discussed by Geist in Refs. 13 and 16. Whereas Ref. 13 provides an equation with adjustable fitting parameters, Ref. 16 provides convenient formulas that are based on detailed numerical modeling of the photodiodes. These formulas do not have adjustable parameters but are normalized to two data points for η_i, one at the blue end of the spectrum and one at the near-infrared end. We attempted to model our data by using both approaches, but we found that neither is ideal for accurately reproducing our data. However, we found that a variation of the approach in Geist *et al.*[13] is quite successful.

1. *Models by Geist and Co-Workers*

The model in Geist *et al.*[13] approximates the effects of recombination loss at the Si–SiO_2 interface by a collection efficiency that increases linearly from a value of P at the interface to a value of unity at a depth T into the photodiode. The value of T is expected to be roughly equal to the distance from the interface to the front of the depletion region. The losses at near-infrared wavelengths are modeled by a term that approximates the internal quantum efficiency distribution in the uniformly doped bulk region behind the depletion region. The complete model equation for the internal quantum efficiency of the photodiode is

Table 3. Values of R_t, $R_t(\lambda_k)$, and η_i

Air Wavelength (nm)	R_t, Measured: Trap 1	R_t, Measured: Trap 2	$R_t(\lambda_k)$: Value	$R_t(\lambda_k)$: Absolute Uncertainty	η_i^a: Trap 1	η_i^a: Trap 2	η_i Uncertainty (%)
406.74	0.01027	0.01051	0.01012	0.00020	0.98532	0.98577	0.035
441.57			0.00626	0.00012	0.99150	0.99185	0.031
487.99			0.00434	0.00007	0.99532	0.99577	0.031
514.53			0.00381	0.00006	0.99643	0.99671	0.040
532.08	0.00351	0.00363	0.00354	0.00005	0.99704	0.99716	0.042
632.82	0.00270	0.00267	0.00273	0.00003	0.99851	0.99870	0.034
769.64			0.00231	0.00002	0.99867	0.99892	0.029
828.30			0.00222	0.00001	0.99868	0.99881	0.027
919.85			0.00211	0.00001	0.99822	0.99829	0.029
950.95			0.00208	0.00001	0.9927	0.9931	0.08

^{a}Values of η_i are determined from the data for η_e (see Table 1) and $R_t(\lambda_k)$.

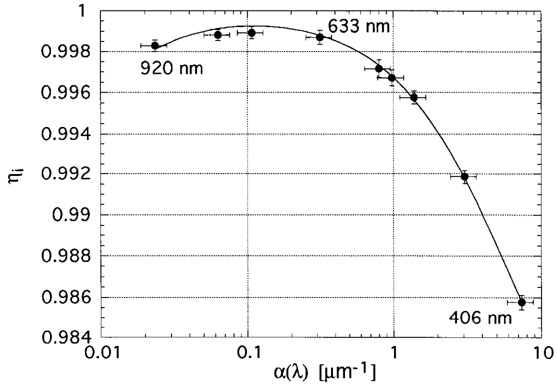

Fig. 5. Results of modeling η_i versus $\alpha(\lambda)$, using the approach of Geist *et al.*[13] The values of η_i for trap detector 2 are shown by filled circles with error bars equal to the uncertainties. The error bars shown for $\alpha(\lambda)$ were estimated from a review of published data (see Appendix A). The solid curve is a fit to Eq. (7). The values of the fitting parameters are $P = 0.9762 \pm 0.0019$, $T = 0.300 \pm 0.04$ μm, and $H = 2.72 \pm 0.20$ mm.

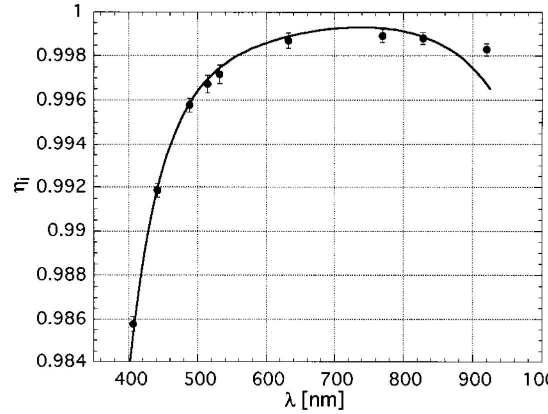

Fig. 6. Results of modeling η_i versus λ, using the approach of Geist *et al.*[16] The values of η_i for trap detector 2 are shown by filled circles with error bars equal to the uncertainties. The solid curve shows the results of using the model of Geist *et al.*[16]

given by

$$\eta_i(\lambda) = P + \frac{1-P}{\alpha(\lambda)T}\{1 - \exp[-\alpha(\lambda)T]\} - \frac{h}{\alpha(\lambda)L^2}\exp[-\alpha(\lambda)H], \tag{7}$$

where $\alpha(\lambda)$ is the absorption coefficient of silicon at wavelength λ, H is the sum of the widths of the front layer and depletion regions, h is the width of the bulk region, and L is the minority carrier diffusion length in the bulk region. T is expected to be roughly comparable with the nominal junction depth (0.21 μm),[17] and $h = 320 \pm 15$ μm.[10] (The specification of distances actually has to be along the direction of travel of the light within the silicon wafer. Although the light is incident upon two out of three photodiodes in the trap detector at an angle of 45°, refraction at the air–Si–SiO_2 interface causes the direction of travel of the light to be within 11° of the normal to the front face. Hence the distance along the light path is within 2% of the distance measured normal to the front face.)

The fitting procedure was carried out with $\alpha(\lambda)$ as the independent variable. The values of $\alpha(\lambda_k)$ were determined by using published data. There are much data for the absorption coefficient available, but the agreement is less than ideal. We chose to use a combination of data from Jellison[18] and a fit by Geist *et al.*[19] of data from Weakliem and Redfield.[20] A review of the data in the literature for the absorption coefficient and the motivation for our choice can be found in Appendix A.

The data for η_i were first fit with P, T, H, and L as adjustable parameters, but we found that this approach led to negative values of H, which is unphysical. Hence we fixed H at a low value (0.5 μm) and fit three parameters; the results are shown in Fig. 5. (The value of H is not critical and the fit was only slightly improved by ignoring the unphysical behavior and using four parameters.) Although the data in the blue region of the spectrum are well fit by this approach, the situation is not so clear at near-infrared wavelengths. Although the deviations at 770 and 828 nm are not more than the uncertainties at these points, it appears that there may be a systematic difference between the shape of the fit and the trend of the data.

We then attempted to model our data by using the approach in Geist *et al.*[16]; the results are shown in Fig. 6. In this case the abscissa is simply wavelength because the analytic form provided in this reference uses wavelength as the independent variable. We normalized the form (according to the method described in Geist *et al.*[16]) by using our data points at 442 and 828 nm. This essentially forces the model to go through the data points at these two wavelengths. These values were chosen because the accuracy of this model is expected to be lower at our end points of 406 and 920 nm. For the data point at 770 nm the difference between the data and the results of this model is similar to that exhibited in Fig. 5. At 920 nm the difference between the model and the data point is quite large, but this model is not expected to be accurate beyond 900 nm. Although this model also yields good results in the blue region of the spectrum, it does not ideally reproduce the data in the near-infrared region.

2. *New Model for the Internal Quantum Efficiency*

Because the results of these models were not completely satisfying, we experimented with other fitting forms. Given the success of the simple form that accurately models the data at the blue end of the spectrum, we chose to model the slight decrease in quantum efficiency at near-infrared wavelengths with the same functional form. This approach was an attempt to obtain the best fit to the data and was not based on the physics of the photodiode. The internal quantum efficiency is given by[21]

$$\eta_i(\lambda) = \int_0^h \exp[-\alpha(\lambda)x]\alpha(\lambda)P(x)\mathrm{d}x, \tag{8}$$

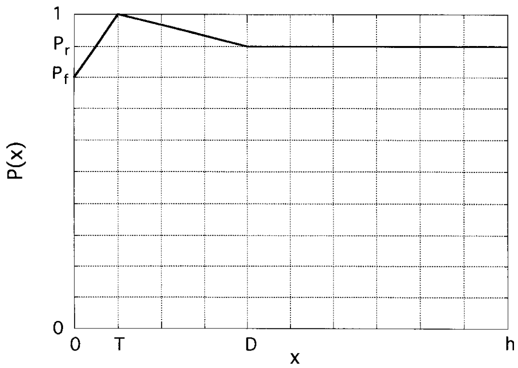

Fig. 7. Model for the variation of collection efficiency $P(x)$ with depth x into the photodiode. Parameters P_f, T, P_r, D, and h are discussed in text.

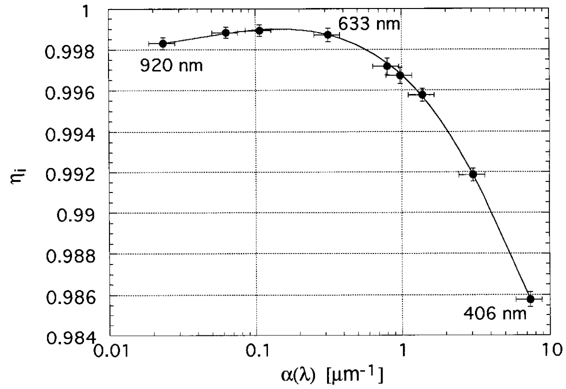

Fig. 8. Results of modeling η_i versus λ, using the new model described in text. The values of η_i for trap detector 2 are shown by filled circles with error bars equal to the uncertainties. The uncertainty shown for $\alpha(\lambda)$ was estimated from a review of published data (see Appendix A). The solid curve shows the results of a fit to Eq. (9) and is also the final result for $\eta_i(\lambda)$. The values of the fitting parameters are $P_f = 0.9757 \pm 0.0018$, $T = 0.289 \pm 0.04$ μm, $P_r = 0.99776 \pm 0.0008$, and $D = 29 \pm 19$ μm.

where $P(x)$ is the collection efficiency at a depth x into the photodiode. The model for the variation of the collection efficiency with depth into the photodiode is shown in Fig. 7. Evaluating Eq. (8) with this form for $P(x)$ yields

$$\begin{aligned}\eta_i(\lambda) = P_f + \frac{1 - P_f}{\alpha(\lambda)T}\{1 - \exp[-\alpha(\lambda)T]\} \\ - \frac{1 - P_r}{\alpha(\lambda)[D - T]}\{\exp[-\alpha(\lambda)T] - \exp[-\alpha(\lambda)D]\} \\ - P_r \exp[-\alpha(\lambda)h], \qquad (9)\end{aligned}$$

where the four fitting parameters, P_f, T, P_r, and D, are defined in Fig. 7. P_f and T correspond to P and T in Eq. (7); hence the first two terms in Eq. (9) originate in the linear increase in the collection efficiency from value P_f at the oxide interface to value 1 at a depth T into the photodiode. The next term originates in the linear decrease in the model collection efficiency from value 1 at a depth T to value P_r at a depth D.

The last term represents the loss caused by light exiting (or being absorbed) at the back end of the photodiode and can be dropped if nearly all of the light is absorbed before reaching the back end. [This term was absent in Eq. (7).] The contribution of this term to the value of η_i increases from 0.06% at 920 nm to 0.8% at 950 nm, and clearly its exact value at any wavelength in this region will be sensitive to the accuracy with which the absorption coefficient is known (see Appendix A). We found that this term was not required for the fit to pass through the data point at 920 nm.

The results of a fit to Eq. (9), but with the last term dropped, are shown in Fig. 8. The agreement is improved over the previous models. The values of the fitting parameters are $P_f = 0.9757 \pm 0.0018$, $T = 0.289 \pm 0.04$ μm, $P_r = 0.99776 \pm 0.0008$, and $D = 29 \pm 19$ μm. The values of P_f and T are very similar to those obtained by using the model of Geist *et al.*,[13] which is expected because these values are strongly constrained by the data at short wavelengths. The value of T is roughly comparable with the nominal junction depth of 0.21 μm. Although the value of D is not well determined, the quality of the fit is significantly decreased if it is fixed at a dramatically different value (such as 3 μm or 300 μm). However, it is unclear whether any physical significance can be associated with parameters P_r and D. Nevertheless, this model accurately reproduces the data and provides a smooth curve for interpolating between the data. Using $R_t(\lambda)$ and $\eta_i(\lambda)$, which are shown by solid curves in Figs. 4 and 8, respectively, we determined $\eta_e(\lambda)$ over the range from 406 to 920 nm; these final results are shown in Fig. 2. The agreement with the original data for η_e is also excellent.

The question remains as to the accuracy and uniqueness of this model. We experimented with variations of the collection efficiency model shown in Fig. 7, including a model with a simple linear drop in $P(x)$ from $x = T$ to $x = h$, a model with $P(x)$ fixed equal to 1 (or some adjustable value) from $x = T$ to $x = D$ and a linear drop from $x = D$ to $x = h$, and other variations. No other model fit the data as well as the model shown in Fig. 7, including some models with five parameters. Unfortunately, we could not find a three-parameter model that yielded results comparable with those shown in Fig. 8.

If the model of Fig. 7 had a rigorous physical basis, we could determine the accuracy by simply testing the effect of varying the fitting parameters by their uncertainties. Although we certainly performed this test, it is possible that other models that may not fit the data as well (but still provide fits that are consistent with the uncertainties in the data) could be equally valid. Hence to establish the accuracy of our model, we determined the variation in the fitted values of η_i for several of the models mentioned above; typically the quality of the fits was somewhere between that shown in Figs. 5 and 8. We also tested the effect of removing certain data points and refitting the data; even when the end points at 406 and

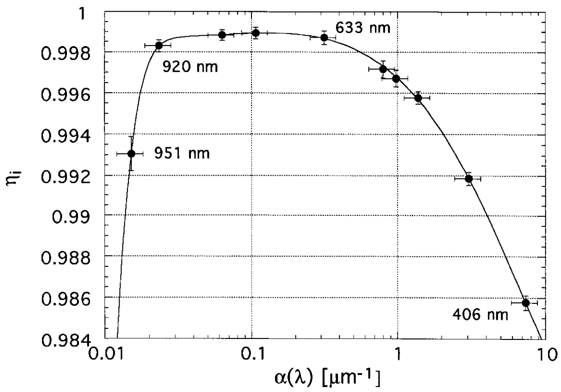

Fig. 9. Results of modeling η_i versus λ, including the data point at 951 nm, with the model described in text. The data for η_i for trap detector 2 are shown by filled circles with error bars equal to the uncertainties. The solid curve is a fit to Eq. (9) with the last term modified as described in the text. The values of the fitting parameters are $P_f = 0.9756 \pm 0.002$, $T = 0.287 \pm 0.04$ μm, $P_r = 0.99849 \pm 0.0005$, $D = 16 \pm 14$ μm, and $R = 0.29 \pm 0.12$.

920 nm were individually removed, the resulting fits were still within 0.03% of the original fit at all wavelengths. From these tests we concluded that the accuracy of the model is $\pm 0.03\%$, throughout the 406-nm to 920-nm range of wavelengths.

The final issue in establishing the accuracy of our model is the effect of using a different data set for $\alpha(\lambda)$. The effect of errors in the data set for $\alpha(\lambda)$ on the results for $\eta_e(\lambda)$ is diluted in a similar way as an error in the trap reflectance: A mapping from λ to $\alpha(\lambda)$ is first used to establish a useful independent variable for the fitting of $\eta_i(\lambda)$, and then the mapping is applied in reverse to reestablish λ as the independent variable for $\eta_e(\lambda)$. Hence errors in the accuracy of $\alpha(\lambda)$ only affect the final results for $\eta_e(\lambda)$ through potential changes in the shape of $\eta_i(\lambda)$. To determine the effect of the rather large uncertainties in $\alpha(\lambda)$ on $\eta_e(\lambda)$, we repeated the modeling of η_i by using two different data sets for $\alpha(\lambda)$. (The two data sets used were from Phillip[22] and the fit in Geist *et al.*[19] of data from Weakliem and Redfield.[20]) The typical change in $\eta_e(\lambda)$ was 0.005% over most of the wavelength range, but it was as high as 0.02% near 406 nm.

3. Extending the Model to 951 nm

So far we have made no attempt to include the data point at 951 nm in our modeling. Although a single, relatively low-accuracy data point does not provide enough information for us to extend our model into this wavelength range, it is interesting to determine if we can reproduce this single point without destroying the excellent agreement shown in Fig. 8. Because the last term in Eq. (9) cannot be neglected at 951 nm, the reflection from the back end of the photodiode must also be taken into account. Because the value of $\exp[-2h\alpha(\lambda)]$ at 951 nm is 0.005% of η_i, essentially no reflected light reaches the junction, so we replace the last term in Eq. (9) by $P_r(1 - R)\exp[-\alpha(\lambda)h]$, where R is the reflectance at the back end of the photodiode. Figure 9 shows the results of fitting all of our data to Eq. (9), with the last term modified in this way. As the reflectance of the back end of the photodiode was not known, it was an additional fitting parameter. The quality of this fit in the 406-nm to 920-nm range is comparable with that of the original model (shown in Fig. 8), and the values of $\eta_i(\lambda)$ agree with those obtained by using the original model to within 0.03%. The values of the fitting parameters are almost all within the uncertainties of the fitting parameters for the original model, and the uncertainties are also comparable with those of the original model. Using 320 μm for the value of h, we find that the fitted value of R is 0.29 ± 0.12. Of course, this fitted value is strongly dependent on the value chosen for h: if instead h is fixed at 305 (335) μm, the fitted value of R is 0.43 ± 0.10 (0.11 ± 0.15) and both of these cases yield reasonable quality fits. (This range for h corresponds to the tolerance on the wafer thickness.) One can equally well fix R and allow h to be fit.

The significance of the results of this five-parameter fit should not be overestimated. The capability of the five-parameter model to fit the data point at 951 nm without significantly disturbing the agreement at all other points is simply related to the rapid increase in the contribution of the last term in Eq. (9) in the range between 920 and 951 nm. Essentially the original four parameters fit the data from 406 to 920 nm, and the fifth parameter, whether it be R or h, fits the point at 951 nm with little effect on the fit between 406 and 920 nm. However, it is encouraging for a future extension of the model that the model fits the data quite well, the parameters are only weakly correlated, and reasonable values are obtained for R if h is fixed at or near its nominal value. More data in this regime will be necessary to investigate the model further.

5. Conclusion

In summary, we have determined the external quantum efficiency of two silicon photodiode light-trapping detectors at nine laser wavelengths between 406 and 920 nm with a combined relative standard uncertainty of 0.03% to 0.04% by using the NIST high-accuracy cryogenic radiometer. We have also determined the reflectance of the trap detectors in this wavelength range, thus permitting the internal quantum efficiency to be extracted from the data. By modeling the internal quantum efficiency, we have determined the external quantum efficiency over the entire 406-nm to 920-nm range with a combined relative standard uncertainty of 0.03%. These two trap detectors will be used to calibrate the working standards of the NIST scale of absolute spectral response.

Appendix A: Review of Data for the Index of Refraction of Silicon

The imaginary part of the index of refraction of silicon has been studied by many researchers.[18–20,22–30] Absorption coefficient $\alpha(\lambda)$ is related to the imaginary part of the index of refraction, $k(\lambda)$, by $\alpha(\lambda) = 4\pi k(\lambda)/$

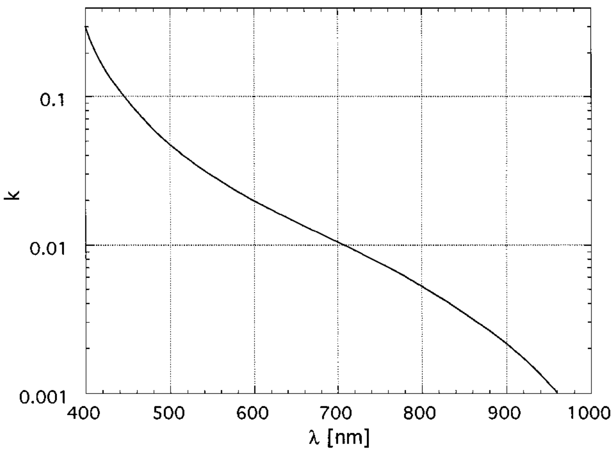

Fig. 10. Values of $k(\lambda)$ for silicon that we have used to determine $\alpha(\lambda)$.

$n\lambda$, where λ is the air wavelength of the light and n is the index of refraction of air. There are several methods for determining the optical constants, including measurements of transmittance and photoconductivity, ellipsometry, and Kramers–Kronig analyses. The goal of this appendix is not to review this complex field, even for the restricted case of silicon between 400 and 950 nm, but rather to compare all the available data, choose a data set, and assign an uncertainty to this choice.

Figure 10 shows the values of $k(\lambda)$ that we have used to determine $\alpha(\lambda)$ in this paper. The curve in Fig. 10 is based on a combination of the results of Jellison[18] (below 650 nm) and those of Geist *et al.*[19] (above 650 nm). The research of Geist *et al.*[19] is a fit of data reported in Weakliem and Redfield[20] and is convenient for the evaluation of $k(\lambda)$ at arbitrary wavelengths. In Fig. 11 we show the deviations of several data sets in the literature from the curve shown in Fig. 10. These data sets were often extracted from graphs in the respective papers, and the

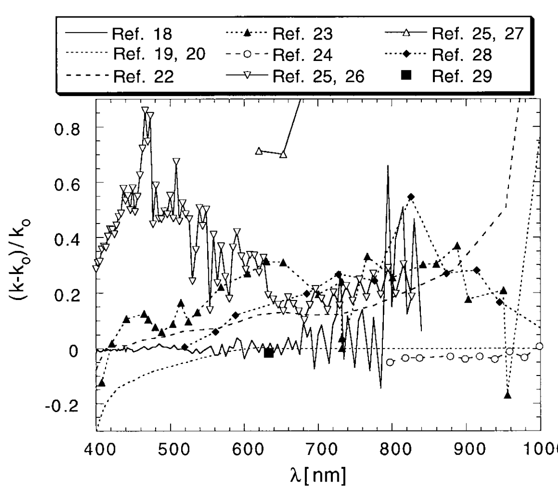

Fig. 11. Relative deviations of several published data sets for $k(\lambda)$ from the values we have chosen (shown in Fig. 10; designated by k_o here).

relative error in the extraction could in some cases be as much as 10%. By definition, the results of Jellison[18] show no deviation below 650 nm and the results of Geist *et al.*[19] show no deviation above 650 nm. (The data of Jellison[18] scatter around zero deviation because we have actually used a fit of that data to generate the smooth curve shown in Fig. 10.) We observe that although there is a group of results that are in a fair agreement, two (from Edwards[25]) noticeably disagree with this group.

The data in Jellison[18] and in Weakliem and Redfield[20] were obtained by the use of different techniques; ellipsometry was used in Jellison[18] and transmittance measurements were used in Weakliem and Redfield.[20] Although transmittance measurements are expected to be the most accurate above 500 nm,[29,30] the need for very thin samples makes this technique more difficult at shorter wavelengths. In Jellison,[18] ellipsometry was used to obtain accurate values in the wavelength region below 650 nm. Hence a combination of the results of these two techniques, with their different respective advantages in different wavelength regimes, seems appropriate. Furthermore, the results of Jellison[18] and Geist *et al.*[19] agree well in the 550-nm to 650-nm region, and they agree well with a recent high-accuracy measurement of $k(\lambda)$ at $\lambda = 633$ nm.[29] Other reasons for this choice are that these results are some of the most recent (although it should be noted that the ellipsometry measurements of Jellison[18] are normalized to the study by Dash and Newman[23]), and the results are available either in tabular form (Jellison[18]) or in an analytical fit to the data (Geist *et al.*[19]). In most of the other references, only semilog plots are provided, from which we extracted the actual data by using a scanner or by hand. As users who are interested in these results, we highly recommend that tables of data should always be provided.

Assigning an uncertainty to the data set for $k(\lambda)$ that we have chosen is a somewhat inexact procedure. We acknowledge that our chosen data set is not in the middle of the group for most of the wavelength range and that other reasonable choices could be made. Leaving aside the data from Edwards,[25] we see that deviations of up to 50% from our choice are apparent in Fig. 11, but 20% is more typical. We have chosen to assign an uncertainty of $\pm 20\%$.

The real part of the index of refraction was only required for the reflectance formula of Born and Wolf.[6] The agreement between the results of Jellison,[18] Phillip,[22] and Edwards[25] for the real part of the index of refraction is better than 2% in the 400-nm to 800-nm wavelength range. For wavelengths shorter than 725 nm, we used the data from Jellison[18] for the real part of the index of refraction of silicon. For wavelengths longer than 725 nm, we used the data of Phillip,[22] but we adjusted these by a scale factor (deviation from unity only 0.2%) so as to match the data of Jellison.[18]

We thank C. Classon for careful measurements of the reflectance and uniformity of the trap detectors and the gain of the transimpedance amplifiers, as well as other contributions to this study. We also acknowledge useful conversations with J. Geist.

References and Notes

1. J. M. Houston, C. L. Cromer, J. E. Hardis, and T. C. Larason, "Comparison of the NIST high accuracy cryogenic radiometer and the NIST scale of detector spectral response," Metrologia **30,** 285–290 (1993).
2. T. R. Gentile, J. M. Houston, J. E. Hardis, C. L. Cromer, and A. C. Parr, "The National Institute of Standards and Technology high-accuracy cryogenic radiometer," Appl. Opt. **35,** 1056–1068 (1996).
3. C. L. Cromer, "A new spectral response calibration method using a silicon photodiode trap detector," presented at the 1991 Measurement Science Conference, Anaheim, Calif., 31 January–1 February 1991.
4. N. P. Fox, "Trap detectors and their properties," Metrologia **28,** 197–202 (1991).
5. M. Stock, J. Fischer, R. Friedrich, H. J. Jung, R. Thornagel, G. Ulm, and B. Wende, "Present state of the comparison between radiometric scales based on three primary standards," Metrologia **30,** 439–449 (1993).
6. M. Born and E. Wolf, *Principles of Optics* (Pergamon, New York, 1980), pp. 632–633.
7. J. E. Martin, N. P. Fox, and P. J. Key, "A cryogenic radiometer for absolute radiometric measurements," Metrologia **21,** 147–155 (1985).
8. F. Lei and J. Fischer, "Characterization of photodiodes in the UV and visible spectral region based on cryogenic radiometry," Metrologia, **30,** 297–303 (1993).
9. R. Kohler, R. Goebel, and R. Pello, "Report on the international comparison of spectral responsivity of silicon detectors," Rapport BIPM-94/9, doc. CCPR/94-2 (Bureau International des Poids et Mesures, Pavillon de Breteuil, 93212 Sevres, Cedex, France).
10. Model 1337-1010BQ, Hamamatsu Corporation, 360 Foothill Rd., P.O. Box 6910, Bridgewater, N.J. 08807-0910. Certain trade names and company products are mentioned in the text or identified in an illustration to specify adequately the experimental procedure and equipment used. In no case does such identification imply recommendation or endorsement by the National Institute of Standards and Technology, nor does it imply that the products are necessarily the best available for the purpose.
11. R. Kohler, R. Goebel, R. Pello, and J. Bonhoure, "Effects of humidity and cleaning on the sensitivity of Si photodiodes," Metrologia **28,** 211–215 (1991).
12. B. N. Taylor and C. E. Kuyatt, "Guidelines for evaluating and expressing the uncertainty of NIST measurement results," NIST Tech. Note 1297 (National Institute of Standards and Technology, Gaithersburg, Md., 1994).
13. J. Geist, E. F. Zalewski, and A. R. Schaefer, "Spectral response self-calibration and interpolation of silicon photodiodes," Appl. Opt. **19,** 3795–3799 (1980).
14. I. H. Malitson, "Interspecimen comparison of the refractive index of fused silica," J. Opt. Soc. Am. **55,** 1205–1209 (1965).
15. P. R. Bevington, *Data Reduction and Error Analysis for the Physical Sciences* (McGraw-Hill, New York, 1969), Chaps. 10 and 11.
16. J. Geist, D. Chandler-Horowitz, A. M. Robinson, and C. R. James, "Numerical modeling of silicon photodiodes for high accuracy applications, Parts I, II, and III," J. Res. Natl. Inst. Stand. Technol. **96,** 463–492 (1991).
17. J. Geist and H. Baltes, "High accuracy modeling of photodiode quantum efficiency," Appl. Opt. **28,** 3929–3939 (1989).
18. G. E. Jellison, Jr., "Optical functions of silicon determined by two-channel polarization modulation ellipsometry," Opt. Mater. **1,** 41–47 (1992).
19. J. Geist, A. Migdall, and H. P. Baltes, "Analytic representation of the silicon absorption coefficient in the indirect transition region," Appl. Opt. **27,** 3777–3779 (1988).
20. H. A. Weakliem and D. Redfield, "Temperature dependence of the optical properties of silicon," J. Appl. Phys. **50,** 1491–1493 (1979).
21. J. Geist, "Quantum efficiency of the p-n junction as an absolute radiometric scale," Appl. Opt. **18,** 760–762 (1979).
22. H. R. Phillip, "Influence of oxide layers on the determination of the optical properties of silicon," J. Appl. Phys. **43,** 2835–2839 (1972).
23. W. C. Dash and R. Newman, "Intrinsic optical absorption in single-crystal germanium and silicon at 77 K and 300 K," Phys. Rev. **99,** 1151–1155 (1955).
24. A. A. Vol'fson and V. K. Subashiev, "Fundamental absorption edge of silicon heavily doped with donor or acceptor impurities," Sov. Phys. Semicond. **1,** 327–332 (1967).
25. D. E. Edwards, "Silicon (Si)," in *Handbook of Optical Constants of Solids* (Academic, New York, 1985), pp. 547–569.
26. D. E. Aspnes and J. B. Theeten, "Spectroscopic analysis of the interface between Si and its thermally grown oxide," J. Electrochem. Soc. **127,** 1359–1365 (1980).
27. R. Hulthen, "Optical constants of epitaxial silicon in the region 1–3.3 eV," Phys. Scr. **12,** 342–344 (1975).
28. R. Braunstein, A. R. Moore, and F. Herman, "Intrinsic optical absorption in germanium-silicon alloys," Phys. Rev. **109,** 695–710 (1958).
29. J. Geist, A. R. Schaefer, J. F. Song, Y. H. Wang, and E. F. Zalewski, "An accurate value for the absorption coefficient of silicon at 633 nm," J. Res. Natl. Inst. Stand. Technol. **95,** 549–558 (1990).
30. G. E. Jellison, Jr. and F. A. Modine, "Optical constants for silicon at 300 and 10 K determined from 1.64 to 4.73 eV by ellipsometry," J. Appl. Phys. **53,** 3745–3753 (1982).